Enhanced Lifetime of Excitons in Nonepitaxial Au/CdS Core/Shell Nanocrystals

Scott Lambright,[†,§] Evgeniia Butaeva,[†,‡] Natalia Razgoniaeva,[†,§] Thomas Hopkins,[‡] Bryan Smith,[‡] Dimuthu Perera,[§] Jonathan Corbin,[‡] Elena Khon,[†,§] Rebekah Thomas,[§] Pavel Moroz,[†,§] Andrey Mereshchenko,[†,‡] Alexander Tarnovsky,[†,‡] and Mikhail Zamkov[†,§,*]

[†]The Center for Photochemical Sciences, [‡]Department of Chemistry, and [§]Department of Physics, Bowling Green State University, Bowling Green, Ohio 43403, United States

ABSTRACT The ability of metal nanoparticles to capture light through plasmon excitations offers an opportunity for enhancing the optical absorption of plasmon-coupled semiconductor materials *via* energy transfer. This process, however, requires that the semiconductor component is electrically insulated to prevent a "backward" charge flow into metal and interfacial states, which causes a premature dissociation of excitons. Here we demonstrate that such an energy exchange can be achieved on the nanoscale by using nonepitaxial Au/CdS core/shell nanocomposites. These materials are fabricated *via* a multistep cation exchange reaction, which decouples metal and semiconductor phases leading to fewer interfacial defects. Ultrafast transient absorption measurements confirm that the lifetime of excitons in the CdS shell ($\tau \approx 300$ ps) is much longer than lifetimes of excitons in conventional, reduction-grown Au/CdS heteronanostructures. As a result, the energy of metal nanoparticles can be efficiently utilized by the semiconductor component without undergoing significant nonradiative energy losses, an important property for catalytic or photovoltaic applications. The reduced rate of exciton dissociation in the CdS domain of Au/CdS nanocomposites was attributed to the nonepitaxial nature of Au/CdS interfaces associated with low defect density and a high potential barrier of the interstitial phase.

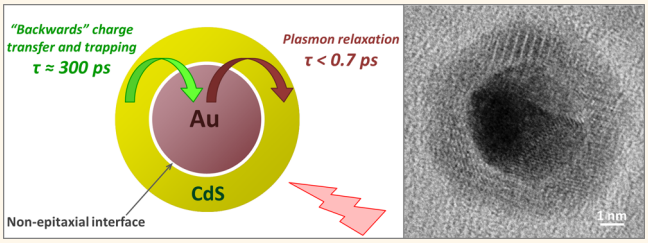

KEYWORDS: photovoltaics · catalysis · nanocrystals · quantum dots

Metal–semiconductor (M–S) heterostructures have long been of interest to fundamental sciences and device engineering applications due to the unique interaction of the two material phases through the formation of the space-charge layer.[1] It was not until recently, however, that the growing ability to fabricate M–S heterostructures on the nanoscale opened up new and far-reaching opportunities for the development of multifunctional composites with properties that cannot be obtained in the bulk phase. This stimulated a great deal of interest in the synthesis of M–S nanostructures exhibiting quantum confinement of electrical charges. As a result, in just the past decade, the scientific community has witnessed the advent of novel M–S nanocomposite architectures, including metal-core/semiconductor-shell heterostructures,[2–4] metal-tipped semiconductor nanocrystals (NCs),[5–15] organically and nonepitaxially[2,16–18] coupled metal–semiconductor composites, and metal cages grown onto semiconductor quantum dots.[19,20] Most of these structures have shown promise for the conversion of energy on the nanoscale, with potential applications in areas of photovoltaics and solar fuel production,[21–26] lasers,[27] light-emitting diodes,[28] biosensing,[29] and Schottky detectors.[30]

The exchange of the excitation energy in metal–semiconductor nanostructures occurs through two major pathways. One of these processes is the transfer of photoinduced charges from the semiconductor (S) to the metal (M) domain, which results in the dissociation of S excitons. In this case, the quantum confinement of electrical charges in the S domain could be used to controllably tune the driving force at S/M interfaces, potentially leading to enhanced transfer rates. As a result, M–S nanocomposites featuring fast photoinduced charge

* Address correspondence to zamkovm@bgsu.edu.

Received for review August 14, 2013 and accepted December 10, 2013.

Published online December 10, 2013
10.1021/nn404264w

transfer and long excited state lifetimes are often explored toward photocatalytic applications, such as H_2 generation.[24] The other mechanism of energy exchange in M−S nanostructures is the interaction between semiconductor excitons and surface plasmons of the M counterpart, which results from the modification of the exciton dipole moment due to local electromagnetic modes of plasmons.[31−33] This interaction is likewise enabled by the quantum confinement of electrical charges and has a unique effect on optoelectronic properties of a composite M−S system. In particular, the excited energy of S and M domains can be efficiently shared though the mechanisms of Förster resonance energy transfer (FRET), Rabi oscillations, or radiative dipole−dipole interaction. Owing to these benefits, exciton−plasmon interactions in M−S nanostructures have been actively explored toward the enhancement of S radiative rates,[34,35] for light-emitting device applications[22,23,36−42] or for increasing the absorption cross section in photovoltaic materials.[21,43]

It would seem that the two main processes of energy exchange in M−S nanocomposites can be readily controlled by adjusting the structural morphology of incorporated domains. However, a number of recent studies have reported rather unusual dynamics of ultrafast energy relaxation in these systems.[44−48] In particular, the decay of photoinduced charges in M−S nanocomposites had been argued to primarily mirror the structure of the interfacial region and not the excited state dynamics of isolated M and S domains.[44] A possible explanation of these results is related to the fact that when the size of M−S nanocomposites falls below the quantum confinement lengths, the interface between the two materials starts to play an important and sometimes defining role. For these materials, interfacial regions occupy a large volume fraction, where the material composition can become markedly different from that of original S and M phases. A characteristic example illustrating such behavior is provided by the recently observed suppression of plasmon and exciton features in Au/CdS matchstick-shaped nanocomposites, grown by means of the oleylamine-mediated reduction of Au salt on the surface of CdS nanorods.[44] The reported changes in the electron dynamics of CdS and Au domains were found to be consistent with the formation of interfacial defect states, which capture photoinduced charges. In particular, the trapped charges manifest themselves through the onset of the photoinduced absorption and simultaneous reduction in the amplitude of both plasmon and exciton absorption features. One of the possible strategies to avoid the formation of such interfacial states relies on using stress-mediating spacer molecules at the junction of the S and M components. While this approach preserves the quantum features of isolated domains, its benefits come at a high cost of weakening the exciton−plasmon coupling, as molecular spacers substantially increase the interparticle distance.

Recently, a new synthetic strategy was developed for curbing the formation of interfacial defects in chemically grown M−S nanocomposites.[2] The reported technique employed a cation exchange reaction in metal nanoparticles to convert a fraction of the M lattice into a semiconductor phase. In contrast to previously developed M−S growth strategies, the aforementioned approach gives rise to nonepitaxial associations at the interfaces of M and S components, which enables direct coupling of unstrained Au and CdS domains through a core/shell morphology (see Figure 1, right panel). Owing to the reduced probability of strain-related interfacial defects, the resulting nanocomposites represent a suitable model system for studying exciton−plasmon interactions in a close-coupling regime. It is expected that once the energy relaxation in the M−S system is not dominated by defect carrier trapping, it can potentially exhibit correlated energy exchange between M and S domains.

Here, we employ ultrafast transient absorption spectroscopy to probe the nature of exciton−plasmon dynamics in nonepitaxial Au/CdS core/shell heteronanocrystals. The hybrid interface of metal and semiconductor domains in these structures was designed to prevent an excessive lattice strain. As a result, the rate of carrier trapping on defect sites was found to be substantially reduced (lifetime, $\tau \approx 300$ ps) in comparison with that of Au/CdS heterostructures grown *via* a conventional, Au-salt reduction approach ($\tau < 0.02$ ps).[49] It is hypothesized that unusually long lifetimes of excitons in nonepitaxial Au/CdS NCs can be

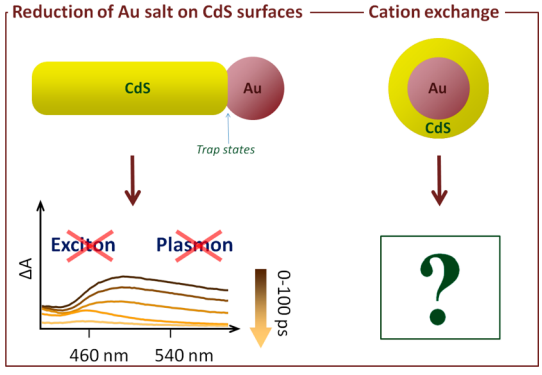

Figure 1. The left panel illustrates the structure of Au/CdS matchstick nanostructures grown *via* the reduction of Au salt on semiconductor nanorod facets. Depending on the specifics of the synthesis, the resulting composites may acquire a large density of interfacial defects, which leads to the suppression of exciton and plasmon features[44] (as indicated in ultrafast transient absorption spectra). The right panel shows the Au/CdS core/shell morphology fabricated using the cation exchange strategy. These materials are expected to show fewer interfacial defects, which suppresses defect trapping, potentially increasing the portion of the absorbed energy that is being shared between the two materials.

attributed to the existence of a significant potential barrier at the boundary of Au and CdS phases, which prevents a "backward" flow of charges into the metal domain.

The observed suppression of carrier trapping in nonepitaxial Au/CdS nanocomposites has several important implications to the development of hybrid nanoscale systems. First, a direct coupling of metal and semiconductor domains is likely to promote exciton−plasmon interactions without unwanted side reactions of charge transfer and defect-localized energy dissipation. A remarkably long lifetime of excitons in the semiconductor shell is also beneficial to catalytic applications of these materials, as the photoinduced charges remain excited long enough to be dissociated at the surface/catalyst interface. Second, in the demonstrated core/shell geometry, the semiconductor domain remains open for the surface functionalization. This allows for the excitation energy absorbed by plasmon oscillations of a M counterpart to be transferred to an appropriate surface moiety. Finally, the observation of reduced carrier trapping in nonepitaxial Au/CdS systems implies that optical excitations result in fewer thermal losses than in the case of reduction-grown M−S nanocomposites where the number of interface-coupled decay channels is greater.

RESULTS AND DISCISSION

The synthesis of nonepitaxial Au/CdS core/shell heteronanocrystals was accomplished using a cation exchange approach (see Methods section for details). Earlier reports of this synthetic strategy utilizing aqueous surfactants[2] provided an adequate control of the core/shell morphology but suffered from the complexity of multiple steps involved in the 24−48 h procedure. In the present study, the synthesis of Au/CdS nanoparticles was simplified through the use of oleylamine as the primary surfactant for each synthetic step, which allowed reducing the overall growth time down to 2 h.

According to the scheme in Figure 2, the synthesis of Au/CdS core/shell NCs involves four main steps:[2] (1) growth of 6−16 nm Au nanocrystals, (2) overcoating of Au dots with a Ag metal shell which exhibits soft Lewis acidity, (3) conversion of a Ag layer into an amorphous Ag_2S silver compound, which in the final step (4) undergoes a cation exchange reaction to form a CdS shell, thus completing the growth of the Au/CdS core/shell nanocomposite. Unlike previously reported protocols,[2,16] Au nanocrystals were grown by thermal decomposition of the gold salt in oleylamine, which leads to the formation of nearly monodisperse nanoparticles exhibiting a plasmon resonance around λ = 525 nm. The key benefit of this approach lies in the surface functionalization of Au nanocrystals with OLAM molecules, which is a suitable surface ligand for the subsequent deposition of the Ag shell. The latter was deposited *via* the thermal reduction of $AgNO_3$ on Au surfaces using oleylamine as both the reaction solvent and the capping agent.[48] Dropwise addition of the silver precursor was essential for suppressing the formation of isolated Ag nanoparticles at this stage, as detailed in the experimental section. The morphology of an intermediate Au/Ag core/shell heterostructure was substantiated based on steady-state optical measurements and transmission electron microscopy analysis. According to Figure 3k,l, the addition of Ag precursor results in the gradual blue-shift of the Au plasmon peak from its original position at λ = 525 nm toward the plasmon resonance of a Ag nanoparticle at λ = 415 nm, indicating the formation of the silver shell. The shift of the plasmon resonance was sometimes accompanied by the onset of a sharp absorption peak at λ = 415 nm in the growth solution of Au/Ag nanocrystals (high energy peak in Figure 3l). This feature reflects the presence of isolated Ag nanoparticles in solution, which can be removed through size-selective precipitation.

TEM images of Au/Ag nanocrystals in Figure 3b,g confirm the formation of a uniform silver layer on the surface of Au. The use of low temperatures during growth has been reported to effectively prevent the formation of an Au/Ag alloy, which tends to form when the reaction mixture is heated to about 250 °C.[48] The core/shell morphology of fabricated nanoparticles can be seen in a characteristic high-resolution TEM image (Figure 3g). Isolated Ag nanoparticles forming during the shell growth step were removed using size-selective precipitation. Following the growth of the Ag shell, the silver layer was converted into a Ag_2S compound by reacting an oleylamine solution of nanoparticles with sulfur at room temperature. In this case, the

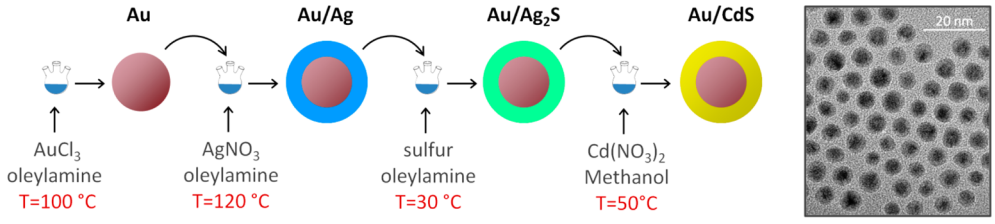

Figure 2. An illustration of the four steps involved in the synthesis of Au/CdS nanocrystals. Oleylamine is used as the primary ligand throughout all reaction stages. The TEM image to the right confirms the core/shell morphology of the final product.

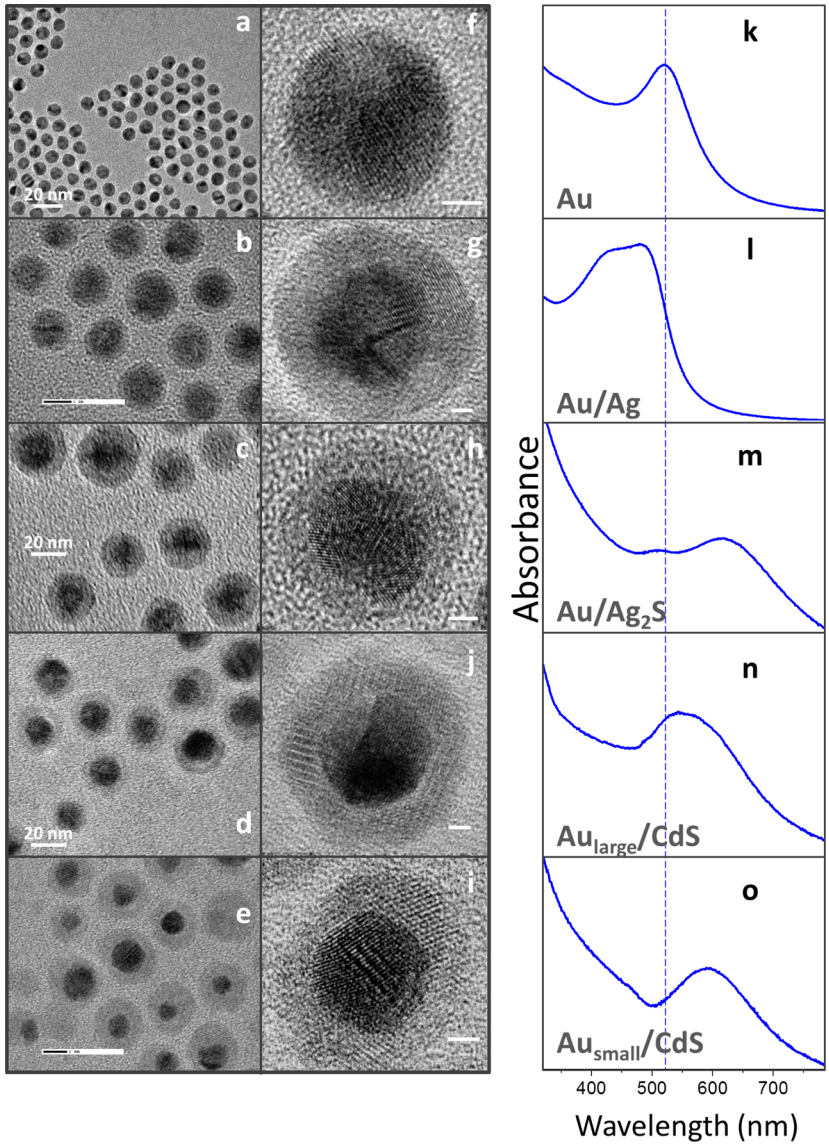

Figure 3. TEM images and absorption spectra of composite nanocrystals formed during each of the four reaction stages involved in the growth of the Au/CdS heteronanocrystals. TEM images are shown for (a and f) Au, (b and g) Au/Ag core/shell nanocrystals, (c and h) Au/Ag_2S core/shell nanoparticles, (c and h) Au/Ag_2S core/shell nanoparticles, (d and j) Au/CdS nanocrystals featuring a 16.1-nm core domain (CdS thickness ≈ 4.1 nm), (e and i) Au/CdS nanocrystals featuring a 6.5-nm core domain (CdS thickness ≈ 3.9 nm). The scale bar in high-resolution TEM images is 1 nm. Steady-state absorption spectra is shown for (k) Au, (l) Au/Ag, (m) Au/Ag2S, (n) Au_{large}/CdS, (o) Au_{small}/CdS.

changes in the shell composition were accompanied by the gradual red-shift of the plasmon resonance from 485 to 630 nm, as expected from Mie theory[50] due to screening of the Au domain by a high-epsilon Ag_2S layer.

In the final step of the growth sequence, the Ag_2S shell was converted into a crystalline CdS layer by means of the $2Ag^+ \rightarrow Cd^{2+}$ cation exchange reaction (see step 4 in Figure 2). According to high-resolution TEM images in Figure 3j,i, and Figure SF1b, the arrangement of Au and CdS domains in resulting Au/CdS heteronanocrystals was consistent with core/shell morphology. A uniform, nonsegmented, placement of the shell material around the core indicates the existence of a minimal lattice strain between the two dissimilar domains. The growth of the CdS shell was accompanied by the onset of weak absorbance feature around 460 nm, corresponding to ground state transitions ($1S_{3/2}h \rightarrow 1Se$) in the semiconductor domain, and the simultaneous blue-shift of the plasmon resonance from λ = 630 to λ = 590 nm due to changes in the surrounding dielectric constant. The presence of both Au and CdS domains in a core/shell structure was likewise confirmed through the observation of characteristic Bragg peak in X-ray powder diffraction (XRD) measurements (see Figure SF1a). Overall, the shapes of Au/CdS nanoparticles were fairly uniform with a standard size deviation of 9.2% and contained less than 3% of CdS impurities (<8% for small-Au samples).

The ultrafast dynamics of photoinduced charges in nonepitaxial Au/CdS heteronanocrystals was

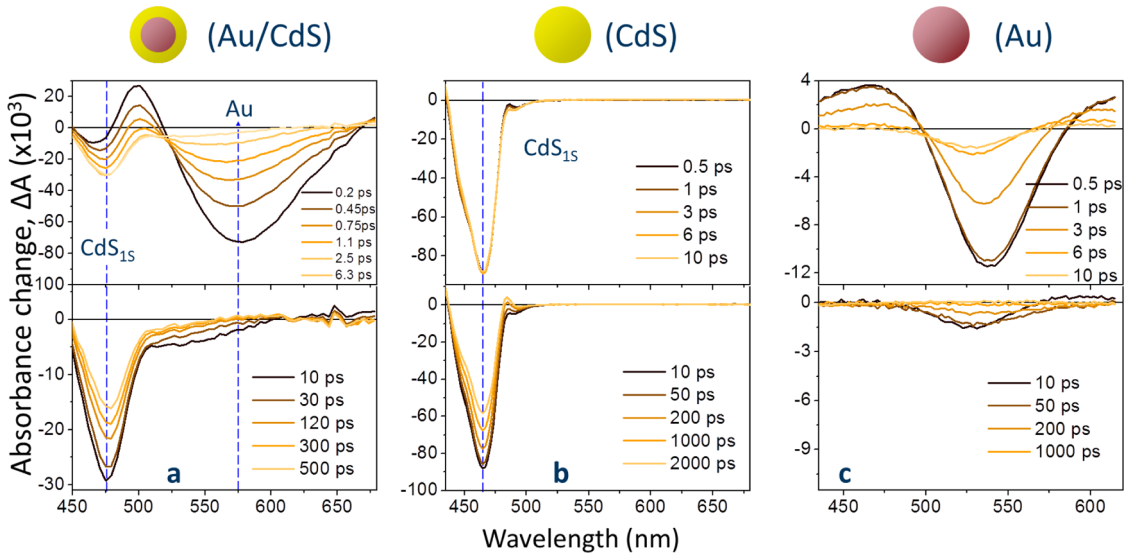

Figure 4. Transient absorption spectra of (a) Au/CdS core/shell nanocomposites, (b) isolated CdS nanocrystals, and (c) 6.0-nm Au nanoparticles. The wavelength of the pump beam (0.09 μJ/pulse) was set to λ = 400 nm in all three cases.

investigated using femtosecond transient absorption spectroscopy. To get a better understanding of energy exchange processes in a core/shell structure, we first examined the dynamics of carriers in isolated Au and CdS nanocrystals. For this purpose, hexane solutions of ≈6-nm gold and 5.2-nm CdS nanoparticles were prepared using standard protocols.[12] The chirp-corrected transient absorption (TA) spectra (Figure 4b), resulting from the excitation of *isolated* CdS nanocrystals with 90-fs laser pulses (λ_{exc}= 400 nm) shows an expected bleach (a negative ΔA region) at λ = 460 nm, corresponding to the ground state 1S(e)−$1S_{3/2}$(h) transitions in these dots. Spectral distortions of TA traces associated with the Stark effect[51] were not observed in the present measurements due to fairly low excitation intensities, which corresponded to the linear power dependence regime. A negligible contribution of the Stark effect into the observed bleach dynamics was likewise consistent with the lack of a positive TA signal at early probe times (τ < 1 ps). In the absence of the Au domain, the recovery of 1S(e)$1S_{3/2}$(h) bleach in CdS is driven primarily by the slow processes of radiative decay and carrier trapping on nanoparticle surfaces. Previous works[52] have demonstrated that the TA bleach of 1S(e)−$1S_{3/2}$(h) transitions in CdS is dominated by photoinduced electrons, as expected due to comparatively low effective masses of these carriers in bulk CdS[53,54] and high degeneracy of hole states in CdS NCs. Consequently, the slow (τ > 2 ns) bleach recovery in isolated CdS NCs was attributed to the decay of 1S electrons *via* processes of recombination and trapping. The observed decay times were consistent with those of previous TA measurements of carrier dynamics in isolated CdS nanorods.[55]

The transient absorption spectra of isolated Au nanoparticles (λ_{exc}= 400 nm, 0.09 μJ/pulse) shows a pronounced bleach in the spectral window of the plasmon resonance ($\lambda \approx$ 530 nm, Figure 4c). This TA feature is characteristic of isolated Au nanoparticles and has been previously attributed to the excitation-induced broadening of the plasmon peak, which causes the TA spectra to form a characteristic "dip" at the plasmon wavelength sandwiched by the two positive "wings".[56,57] Such excitation-induced broadening of the plasmon absorbance in Au nanoparticles has been attributed to both dipolar[58] (Mie theory) as well as nondipolar contributions into plasma oscillations (*e.g.*, quadrupole).[55] It is generally accepted that plasmons in metal nanoparticles undergo a three-step relaxation, which includes femtosecond-scale electron−electron scattering and plasmon dephasing, 1−10 ps electron−phonon energy dissipation,[59] and a slower, >100 ps, energy transfer to the local environment.[60,61] On the basis of the observed time scale of bleach recovery in isolated Au dots, we conclude that hot electrons created by dephasing of plasmons tend to decay through interactions with phonons in these nanoparticles. Furthermore, the double exponential character of the observed relaxation (see Figure SF1) suggests that other relaxation processes exceeding the time scale of electron−phonon interaction, such as the transfer of energy to the surrounding environment, may contribute to the short-time decay in ligand-passivated Au nanoparticles.

The dynamics of exciton−plasmon interactions in domain-coupled Au/CdS heteronanocrystals is examined next. We start our analysis by recalling the results of several recent studies on the ultrafast carrier dynamics in epitaxially grown Au/CdS nanocomposites. These structures are fabricated *via* a chemical reduction of Au salt on tips of CdS nanorods using either oleylamine[12] or dodecyldimethylammonium bromide

(DDAB)[62] reducing agents. Our own study[44] performed on OLAM-capped Au/CdS heterostructures showed a pronounced suppression of the plasmon resonance accompanied by the onset of an enhanced photoinduced absorption feature (positive ΔA). These were attributed to strong coupling of interfacial trap states to electronic wave functions in both M and S domains. Some evidence of the photoinduced absorption along with the reduced amplitude of the plasmon bleach was also seen in a recent TA investigation of Au/PbS nanoparticles.[46] However, in another TA-based study[49] of DDAB-reduced Au/CdS matchstick heterostructures, both plasmon (Au) and exciton (CdS) features were detectable, but very short-lived ($\tau_{exciton} \approx 20$ fs). These results were corroborated by a few other reports of TA dynamics in M/S heterostructures[45,47] which reported some level of interfacial coupling effect on the ultrafast carrier decay but have not seen any definitive signature of the plasmon suppression. In light of these results, we have re-examined the dynamics of epitaxially coupled Au/CdS "nanobarbell" composites using a TA spectroscopy approach. The results of present experiments (see Figure SF3) were found to be in a good agreement with the previous measurements, confirming the suppression of plasmon and exciton features in respective M and S domains. We believe that the origin of the discrepancy in the TA dynamics of seemingly equivalent M−S systems is related to the difference in the morphologies of Au/CdS interfaces that result from dissimilar growth techniques. In particular, the density of interfacial defects might be the key parameter responsible for the "M−S coupling effect" and the associated premature depletion of the excitation energy through side reactions. If this is the case, nonepitaxial composites of Au and CdS materials fabricated *via* a cation-exchange growth strategy should provide a proper model system for testing this hypothesis.

Figure 4 summarizes the TA dynamics of nonepitaxial Au/CdS heteronanocrystals, featuring a small Au core ($d \approx 6.2$ nm) and 4.5-nm CdS shell. The early time spectra, presented in the top portion of the figure, shows two pronounced bleach areas at $\lambda = 575$ and $\lambda = 470$ nm, which correspond to plasmon and exciton features in Au and CdS domains, respectively. Spectral profiles of these excitations appear to be similar to those of isolated Au (Figure 4c) and CdS domains (Figure 4b), indicating that nonlinear distortion of the TA spectra due to M−S coupling is diminished compared to the case of reduction-grown Au/CdS nanocrystals (Figure SF3).[44] Both exciton and plasmon bleach regions persist into the long-time TA spectra (Figure 4a, lower panel) exhibiting decay half-lives of 300 and 0.7 ps, respectively.

The TA dynamics of Au/CdS core/shell nanocomposites shows several important trends. First, the broad-band photoinduced absorption in these structures appears to be much weaker than in the case of epitaxially grown Au/CdS nanobarbells (Figure SF3a). The suppressed photoinduced absorption amplitude in core/shell nanostructures provides indirect evidence that trapping of photoinduced charges in interfacial states is no longer the dominant process of carrier decay. Indeed, if the density of interfacial states was comparable or greater than that of zero-angular momentum excited states, filling of traps by hot electrons would have been reflected in the early time spectra as a broad-band positive TA signal. However, this is not the case for core/shell structures, where the $\tau = 0.5-5$ ps time window is dominated by two negative bleach regions. The second unique trend observed for Au/CdS core/shell structures is the unsuppressed plasmon resonance in 6.2-nm gold domains, which are small enough to show suppression in reduction-grown Au/CdS nanobarbells.[44] This behavior is likewise consistent with the low density of interfacial traps.

While charge scattering on interfacial defects appears to be minimal for Au/CdS core/shell NCs, the observed kinetic traces of bleach recovery are markedly different from those of isolated Au and CdS domains. The comparison of kinetic curves in Figure 5 reveals that the CdS bleach recovers faster when

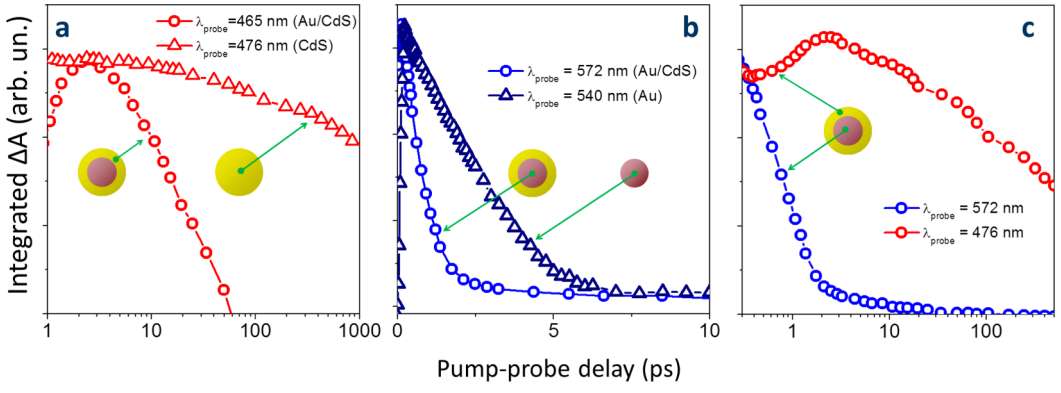

Figure 5. Temporal evolution of the TA beach recovery for (a) CdS band edge excitons ($\lambda \approx 460-480$ nm) in Au/CdS (circles) and isolated CdS nanocrystals (triangles), (b) Au plasmons in Au/CdS (circles) and isolated Au nanocrystals (triangles), (c) CdS band edge excitons (red) and Au plasmons (blue) in Au/CdS nanocomposites.

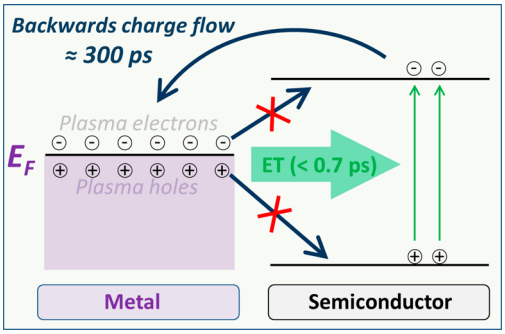

Figure 6. An illustration of energy redistribution processes in nonepitaxial core/shell NCs. Within 0.7 ps of the excitation, half of the excitation energy of the metal core is dissipated, partly through the generation of electron−hole pairs in the CdS shell. The backward flow of excited electrons into Au or interfacial traps occurs on a slower time scale with a characteristic half-life of 300 ps.

coupled to the Au domain. In light of the fact that the primary contribution into the TA bleach of CdS is due to filling of electronic states in the conduction band, we conclude that CdS−Au coupling in core/shell nanoparticles promotes a 300-ps transfer of photoinduced charges from the 1S state of CdS to unoccupied levels of Au, as illustrated in Figure 6. The energy transfer from the CdS shell to a Au core is also possible, however, a recent study[48] has found that the contribution of this process in semiconductor-metal heteronanocrystals is comparatively small. Therefore, the charge transfer to metal is believed to be the primary mechanism of exciton decay. It should be noted that the photoinduced electrons in CdS shell can likewise be transferred to defect states at the Au/CdS interface, which would result in the dissociation of an exciton and the ensuing recovery of a TA bleach. The relative contribution of this process, however, cannot be evaluated in this study.

Another important trend revealed by the comparison of kinetic traces in Figure 5 is the accelerated recovery of the plasmon resonance in the Au domain caused by the presence of the CdS shell. The direct transfer of excited charges from the Au domains into the CdS shell is intrinsically inefficient due to the low-energy character of plasma oscillations in metals (see Figure 6). However, there are several other decay processes that can contribute to the enhanced relaxation rate of excited electrons in the metal core. One likely mechanism is the cooling of hot electrons in Au through interactions with the phonons of the CdS lattice. This type of electron−phonon energy exchange would result in heating of the semiconductor shell, and therefore will not affect the TA dynamics of CdS excitons. The typical time scale for such electron−phonon assisted decay is in the several picoseconds range, which falls within the confines of the observed decay time window. The other mechanism which can explain the accelerated decay of plasmons in Au domains is the relaxation of hot carrier population *via* the energy transfer to the external environment. While the direct transfer of plasmon energy (≈2.1 eV) to band gap excitons (≈2.7 eV) is not energetically accessible, hot carriers in the Au domain could still relax through the generation of excited pairs at defect states of the interfacial region as well as the CdS lattice. Furthermore, the decay of hot electrons in the metal core appears to be correlated with the delayed rise of CdS bleach (see Figure 5a, $\tau \approx 2.5$ ps), which may indicate the metal-to-semiconductor energy transfer. Further studies focusing on the nature of such energy exchange, especially under resonant excitation conditions will be needed to confirm this claim. We note that to evaluate the contribution from excitons in Au/CdS core/shell nanoparticles, the contribution from Au domains was excluded. To this end, the positive TA contribution originating from hot carriers in Au was fitted and subtracted from the signal. The residual negative bleach corresponding to the ground state exciton in CdS was then integrated over the 440−500 nm range.

It should be stressed that the most significant outcome of present measurements is the observation of reduced carrier trapping on interfacial states of nonepitaxial Au/CdS nanocomposites. As illustrated in Figure 6, a photoinduced charge transfer from CdS into interfacial trap states or the electron levels of Au takes 300 ps, several orders of magnitude longer than in reduction-grown Au/CdS heteronanocrystals. This provides indirect evidence of two important structural features that define the carrier dynamics in nonepitaxial core/shell nanocrystals: (i) the density of interfacial defects is relatively small corresponding to the trapping rate of no greater than $\Gamma < 1/300$ ps, and (ii) Au and CdS domains are separated by a potential barrier, which reduces the rate of otherwise energetically favorable CdS-to-Au charge transfer.

CONCLUSIONS

Femtosecond transient absorption spectroscopy was used to investigate the nature of excited state dynamics in Au/CdS core/shell nanocomposites. These nanostructures were fabricated *via* a multistep cation exchange reaction, which decouples metal and semiconductor phases, thereby suppressing the formation of interfacial defects. Our measurements indicate that the ultrafast energy redistribution across Au/CdS nanocomposites benefits from the nonepitaxial nature of Au/CdS interfaces in several ways. First, energy losses on defects are significantly reduced compared to reduction-grown metal−semiconductor nanostructures. The suppression of defect scattering is an important step as it allows for the metal-to-semiconductor energy transfer to unfold before impurity-localized quenching of excitons can occur. As a result, the energy of the Au core can be transferred to a semiconductor

counterpart, potentially enhancing its catalytic or photovoltaic activity. Second, we demonstrate that dissociation of CdS excitons due to charge transfer into Au domain is relatively slow, which points toward the existence of a potential barrier at the Au/CdS interface. This property should likewise favor the catalytic function of the semiconductor component, as it extends the exciton lifetime, increasing the probability of charge transfer into a surface-appended catalyst.

METHODS

Materials. Acetone (ACS, Amresco), silver nitrate (99%, Sigma-Aldrich), gold(III) chloride (99%, Acros Organics), cadmium nitrate tetrahydrate (99.999%, Aldrich), oleylamine (tech., 70%), sulfur (99.999%, Acros), tributylphosphine (TBP) (97%, Aldrich), methanol (anhydrous, 99.8%, Aldrich), ethanol (anhydrous, 95%, Aldrich), and toluene (anhydrous, 99.8%, Aldrich) were used as purchased. All reactions were performed under argon atmosphere using the standard air free Schlenk technique unless otherwise stated. The centrifuge used for precipitation operated at 7200 rpm.

Synthesis of Oleylamine-Capped Au Nanocrystals (NCs). Au NCs were synthesized using a one-pot procedure developed in our group.[12] In a typical synthesis, 0.011 g of $AuCl_3$ was placed in a one-neck flask and dissolved in 3 mL of oleylamine by 10−15 min of sonication. This reaction mixture was orange in color when the Au salt was dissolved in oleylamine, indicating a formation of Au−oleate complexes. While stirring, the temperature of this reaction solution was raised to and maintained at 100 °C for 30 min. During this time, the color of the reaction mixture changed from orange to deep purple. After 30 min of heating, the solution was cooled to room temperature. The reaction mixture was transferred to 2 centrifuge tubes. An excess of ethanol was added to these tubes, which were then centrifuged for 3 min. The clear supernatant was poured off. The Au NCs that had precipitated were dissolved in 6 mL toluene. These NCs were then precipitated a second time with the addition of an excess of ethanol and subsequent centrifugation. The final precipitate was suspended in 4 mL toluene.

Synthesis of Oleylamine-Capped Au/Ag Core/Shell NCs. Ag shells were grown using a procedure inspired by Shore *et al.*[63] In a typical synthesis, Au NCs from the previous step were injected into a one-neck flask, along with 5 mL oleylamine. The temperature of the Au NC/oleylamine solution was raised to and maintained at 120 °C while stirring. Separately, a 1.05×10^{-2} M solution of $AgNO_3$ in deionized water was prepared by sonication. When all toluene had evaporated from the reaction flask, either 0.1 or 0.2 mL of the $AgNO_3$ precursor was injected dropwise into the flask of Au NCs. Each addition of cold water to the reaction mixture and the water's subsequent evaporation would cool the reaction mixture by 10−15 °C. The temperature of the mixture was allowed to reach 120 °C again and then allowed to react for 10 min. Care was taken to control the concentration of Ag^+ ions in the reaction mixture, as a high concentration of Ag^+ would result in isolated Ag nanoparticle nucleation.

Increasing thickness of Ag shells on Au NCs could be tracked by monitoring the nanoparticles' localized surface plasmon resonance (LSPR) peak absorption feature. When using all Au NCs from the previous step, an addition of 0.5 mL (in increments of no more than 0.2 mL per 10 min) of the $AgNO_3$ solution would yield a 15−20 nm blue-shift of the LSPR peak (to about 495−500 nm), whereas adding a total of 0.9 mL of the $AgNO_3$ precursor would result in a 40 nm blue-shift to 475 nm. TEM imaging has shown that Au/Ag NCs with a LSPR peak of 485 nm have a shell thickness of ∼3.5 nm.

After the desired LSPR peak shift was attained, the reaction solution was cooled to room temperature. Excess ethanol was added to the solution, which was then centrifuged. The precipitate was then suspended in ∼4 mL of toluene. If only one LSPR peak was observed in the absorbance profile during the shell growth process, the precipitate was stored. If a second LSPR peak at λ = 415 nm was observed during shell growth, which is indicative of isolated Ag NCs present in the solution, a size selective precipitation procedure was performed to separate the two species of NCs. To this end, ethanol was added to the solution of NCs in increments of 1 mL. After every addition of ethanol, the increasingly polar solution was centrifuged. When some precipitate was observed, a sample was taken from the supernatant. An absorption profile was taken from this sample. If the section of the absorption profile between 400 and 600 nm featured an asymmetric LSPR peak or multiple peaks, another increment of ethanol would be added to the supernatant and the solution was centrifuged again. If a symmetric LSPR peak was observed at ∼415 nm, then it was assumed that the majority of the NCs in the supernatant were isolated Ag NCs, as opposed to Au/Ag core/shell NCs. In this case, the supernatant was discarded and the precipitate was dissolved in 4 mL toluene. An absorption profile was generated from a sample of this refined NC solution.

Conversion of Au/Ag to Au/Ag_2S Core/Shell NCs. The following step was adapted from the techniques reported by Zang *et al.*[2] First, a 1.22×10^{-6} M sulfur/oleylamine soluiton was prepared by sonication under argon. Concurrently, the Au/Ag NCs from the previous procedure were injected into a one-neck flask. The sulfur precursor was added in 0.2 mL increments to the solution of Au/Ag core/shell NCs, which were under argon and being vigorously stirred, and then left to react for 10 min. After 10 min, a sample was taken for spectral analysis. Sulfur was added in this way until the LSPR absorption peak had red-shifted to ∼630 nm. The NCs were then cleaned once by adding 10 mL ethanol to the reaction solution and centrifugating the solution. Under argon, the precipitated NCs were then suspended in 4 mL of toluene.

Conversion of Au/Ag_2S to Au/CdS. The following step was adapted from the techniques reported by Zang *et al.*[2] In a one neck flask, 0.05 g of $Cd(NO_3)_2$ was added to 1.0 mL of methanol and sonicated for 20 min. Separately, the Au/Ag_2S NCs from the previous step in the synthesis were injected into a flask under argon. After sonication, the $Cd(NO_3)_2$ solution and 0.1 mL of TBP were injected into the Au/Ag_2S . The temperature of the reaction mixture was raised to, and maintained at, 50 °C for 45 min under vigorous stirring. The contents of the flask were then cooled to room temperature. Ten milliliters of methanol was added to the reaction mixture, which was subsequently centrifuged. The precipitate was then dissolved and stored in toluene, with a few drops of oleylamine added to the final solution of NCs for colloidal stability.

Characterization. UV−vis absorption and photoluminescence spectra were recorded using a CARY 50 scan spectrophotometer and a Jobin Yvon Fluorolog FL3−11 fluorescence spectrophotometer. High resolution transmission electron microscopy measurements were carried out using JEOL 311UHR operated at 300 kV. Specimens were prepared by depositing a drop of nanoparticle solution in organic solvent onto a carbon-coated copper grid and allowing it to dry in air. X-ray powder diffraction (XRD) measurements were carried out on a Scintag XDS-2000 X-ray powder diffractometer. FL lifetime measurements were performed using a time-correlated single photon counting setup utilizing SPC-630 single-photon counting PCI card (Becker & Hickle GmbH), picosecond diode laser operating at 400 nm, as an excitation source (Picoquant), and an id50 avalanche photodiode (Quantique).

Transient Absorption Spectroscopy. The laser system for transient absorption measurements was described in earlier reports.[64] The setup was based on a Ti:sapphire amplified laser system (Hurricane, Spectra Physics) operating at a repetition rate of 1 kHz and delivering 800-nm 90-fs laser pulses. The laser output

was split into two components: one was directed to the TOPAS-C optical parametric amplifier to produce excitation pulses, and the second was focused onto a CaF2 plate to generate a white-light-continuum for broad-band probe pulses (350−800 nm). All transient absorption data were corrected for the group velocity dispersion of the white-light continuum with an accuracy ±25 fs by using the nonresonant ΔA signals from the neat solvent. The incident excitation pulse was attenuated before the sample position using appropriate neutral density filters to ensure the absence of solvent contribution due to nonlinear pump absorption at time delays equal to or longer than $\Delta\tau$ = 100 fs. Overall, solvent and flow cell windows contributions were found to be negligibly small compared to nanoparticle signals. Linearity of the ΔA was verified by plotting the integrated bleach signal *versus* excitation pulse energy (400 nm pump, 0.09−1 μJ range).

Conflict of Interest: The authors declare no competing financial interest.

Supporting Information Available: Additional transient absorption data. This material is available free of charge *via* the Internet at http://pubs.acs.org.

Acknowledgment. We gratefully acknowledge OBOR "Material Networks" program and NSF Award awards CHE-1112227, and CBET-1236355 for financial support.

REFERENCES AND NOTES

1. Many, A.; Goldstein, Y.; Grover, N. B. *Semiconductor Surfaces*. North-Holland: Amsterdam, 1965.
2. Zhang, J.; Tang, Y.; Lee, K.; Ouyang, M. Nonepitaxial Growth of Hybrid Core-Shell Nanostructures with Large Lattice Mismatches. *Science* **2010**, *327*, 1634–1638.
3. Shi, W.; Zeng, H.; Sahoo, Y.; Ohulchanskyy, T. Y.; Ding, Y.; Wang, Z. L.; Swihart, M.; Prasad, P. N. A General Approach to Binary and Ternary Hybrid Nanocrystals. *Nano Lett.* **2006**, *6*, 875–881.
4. Kim, H.; Achermann, M.; Balet, L. P.; Hollingsworth, J. A.; Klimov, V. I. Synthesis and Characterization of Co/CdSe Core/Shell Nanocomposites: Bifunctional Magnetic-Optical Nanocrystals. *J. Am. Chem. Soc.* **2005**, *127*, 544–546.
5. Mokari, T.; Rothenberg, E.; Popov, I.; Costi, R.; Banin, U. Selective Growth of Metal Tips onto Semiconductor Quantum Rods and Tetrapods. *Science* **2004**, *304*, 1787–1790.
6. Carbone, L.; Kudera, S.; Giannini, C.; Ciccarella, G.; Cingolani, R.; Cozzoli, P. D.; Manna, L. Selective Reactions on the Tips of Colloidal Semiconductor Nanorods. *J. Mater. Chem.* **2006**, *16*, 3952–3956.
7. Saunders, A. E.; Popov, I.; Banin, U. Synthesis of Hybrid CdS−Au Colloidal Nanostructures. *J. Phys. Chem. B* **2006**, *110*, 25421–25429.
8. Menagen, G.; Mocatta, D.; Salant, A.; Popov, I.; Dorfs, D.; Banin, U. Selective Gold Growth on CdSe Seeded CdS Nanorods. *Chem. Mater.* **2008**, *20*, 6900–6902.
9. Carbone, L.; Jakab, A.; Khalavka, Y.; Sonnichsen, C. Light-Controlled One-Sided Growth of Large Plasmonic Gold Domains on Quantum Rods Observed on the Single Particle Level. *Nano Lett.* **2009**, *9*, 3710–3714.
10. Menagen, G.; Macdonald, J. E.; Shemesh, Y.; Popov, I.; Banin, U. Au Growth on Semiconductor Nanorods: Photo-induced *versus* Thermal Growth Mechanisms. *J. Am. Chem. Soc.* **2009**, *131*, 17406–17411.
11. Mokari, T.; Costi, R.; Sztrum, C. G.; Rabani, E.; Banin, U. Formation of Symmetric and Asymmetric Metal−Semiconductor Hybrid Nanoparticles. *Phys. Status Solidi B* **2006**, *243*, 3952–3958.
12. Khon, E.; Hewa-Kasakarage, N. N.; Nemitz, I.; Acharya, K.; Zamkov, M. Tuning the Morphology of Au/CdS Nano-Composites through Temperature-Controlled Reduction of Gold-Oleate Complexes. *Chem. Mater.* **2010**, *22*, 5929–5936.
13. Costi, R.; Saunders, A. E.; Banin, U. Colloidal Hybrid Nanostructures: A New Type of Functional Materials. *Angew. Chem., Int. Ed.* **2010**, *49*, 4878–4897.
14. Schaak, R. E.; Williams, M. E. Full Disclosure: The Practical Side of Nanoscale Total Synthesis. *ASC Nano* **2012**, *6*, 8492–8497.
15. Talapin, D. V.; Yu, H.; Shevchenko, E. V.; Lobo, A.; Murray, C. B. Synthesis of Colloidal PbSe/PbS Core-Shell Nanowires and PbS/Au Nanowire-nanocrystal Heterostructures. *J. Phys. Chem.* **2007**, *111*, 14049–14054.
16. Zhang, J. T.; Tang, Y.; Lee, K.; Ouyang, M. Tailoring Light-Matter-Spin Interactions in Colloidal Hetero-Nanostructures. *Nature* **2010**, *466*, 91–95.
17. Shevchenko, E. V.; Bodnarchuk, M. I.; Kovalenko, M. V.; Talapin, D. V.; Smith, R. K.; Aloni, S.; Heiss, W.; Alivisatos, A. P. Gold/Iron Oxide Core/Hollow-Shell Nanoparticles. *Adv. Mater.* **2008**, *20*, 4323–4329.
18. Lee, J.; Orazbayev, A.; Govorov, A. O.; Kotov, N. A. Solvent Effect in Dynamic Superstructures from Au Nanoparticles and CdTe Nanowires: Experimental Observation and Theoretical Description. *J. Phys. Chem. C* **2010**, *114*, 1404–1410.
19. Yang, J.; Sargent, H.; Kelley, S. O.; Ying, J. Y. A General Phase-Transfer Protocol for Metal Ions and its Application in Nanocrystal Synthesis. *Nat. Mater.* **2009**, *8*, 683–689.
20. Bekenstein, Y.; Vinokurov, K.; Banin, U.; Millo, O. Electronic Properties of Hybrid Cu2S/Ru Semiconductor/Metallic-Cage Nanoparticles. *Nanotechnology* **2012**, *23*, 505710–505716.
21. Bao, N.; Shen, L.; Takata, T.; Domen, K. Self-Templated Synthesis of Nanoporous CdS Nanostructures for Highly Efficient Photocatalytic Hydrogen Production under Visible Light. *Chem. Mater.* **2008**, *20*, 110–117.
22. Elmalem, E.; Saunders, A. E.; Costi, R.; Salant, A.; Banin, U. Growth of Photocatalytic CdSe−Pt Nanorods and Nanonets. *Adv. Mater.* **2008**, *20*, 4312–4317.
23. Berr, M.; Vaneski, A.; Susha, A. S.; Rodríguez-Fernández, J.; Döblinger, M.; Jäckel, F.; Rogach, A. L.; Feldmann, J. Colloidal CdS Nanorods Decorated with Subnanometer Sized Pt Clusters for Photocatalytic Hydrogen Generation. *Appl. Phys. Lett.* **2010**, *97*, 093108–093111.
24. Amirav, L.; Alivisatos, P. A. Photocatalytic Hydrogen Production with Tunable Nanorod Heterostructures. *J. Phys. Chem. Lett.* **2010**, *1*, 1051–1054.
25. Acharya, K. P.; Khnayzer, R. S.; O'Connor, T.; Diederich, G.; Kirsanova, M.; Klinkova, A.; Roth, D.; Kinder, E.; Imboden, M.; Zamkov, M. The Role of Hole Localization in Sacrificial Hydrogen Production by Semiconductor−Metal Heterostructured Nanocrystals. *Nano Lett.* **2011**, *11*, 2919–2926.
26. Morfa, A. J.; Rowlen, K. L.; Reilly, T. H.; Romero, M. J.; van de Lagemaat, J. Plasmon-Enhanced Solar Energy Conversion in Organic Bulk Heterojunction Photovoltaics. *Appl. Phys. Lett.* **2008**, *92*, 013504–013507.
27. Oulton, R. F.; Sorger, V. J.; Zentgraf, T.; Ma, R. M.; Gladden, C.; Dai, L.; Bartal, G.; Zhang, X. Plasmon Lasers at Deep Subwavelength Scale. *Nature* **2009**, *461*, 629–632.
28. Kwon, M. K.; Kim, J. Y.; Kim, B. H.; Park, I. K.; Cho, C. Y.; Byeon, C. C.; Park, S. J. Surface-Plasmon-Enhanced Light-Emitting Diodes. *Adv. Mater.* **2008**, *20*, 1253–1257.
29. Lee, J.; Hernandez, P.; Lee, J.; Govorov, A. O.; Kotov, N. A. Exciton-Plasmon Interactions in Molecular Spring Assemblies of Nanowires and Wavelength-Based Protein Detection. *Nat. Mater.* **2007**, *6*, 291–295.
30. Jestl, M.; Maran, I.; Kock, A.; Beinstingl, W.; Gornik, E. Polarization-Sensetive Surface-Plasmon Schottky Detectors. *Opt. Lett.* **1989**, *14*, 719–721.
31. Nikoobakht, B.; Burda, C.; Braun, M.; Hun, M.; El-Sayed, M. A. The Quenching of CdSe Quantum Dots Photoluminescence by Gold Nanoparticles in Solution. *Photochem. Photobiol.* **2002**, *75*, 591–597.
32. Drexhage, K. H. Interaction of Light with Monomolecular Dye Layers. *Prog. Opt.* **1974**, *12*, 163–232.
33. Achermann, M. Exciton-Plasmon Interactions in Metal-Semiconductor Nanostructures. *J. Phys. Chem. Lett.* **2010**, *1*, 2837–2843.
34. Muskens, O. L.; Giannini, V.; Sanchez-Gil, J. A.; Rivas, J. G. Strong Enhancement of the Radiative Decay Rate of Emitters by Single Plasmonic Nanoantennas. *Nano Lett.* **2007**, *7*, 2871–2875.

35. Wang, Y.; Yang, T.; Tuominen, M. T.; Achermann, M. Radiative Rate Enhancements in Ensembles of Hybrid Metal-Semiconductor Nanostructures. *Phys. Rev. Lett.* **2009**, *102*, 163001–163005.
36. Noginov, M. A.; Zhu, G.; Mayy, M.; Ritzo, B. A.; Noginova, N.; Podolskiy, V. A. Stimulated Emission of Surface Plasmon Polaritons. *Phys. Rev. Lett.* **2008**, *101*, 226806–226810.
37. Noginov, M. A.; Zhu, G.; Belgrave, A. M.; Bakker, R.; Shalaev, V. M.; Narimanov, E. E.; Stout, S.; Herz, E.; Suteewong, T.; Wiesner, U. Demonstration of a Spaser-Based Nanolaser. *Nature* **2009**, *460*, 1110–1112.
38. Zheludev, N. I.; Prosvirnin, S. L.; Papasimakis, N.; Fedotov, V. A. Lasing Spaser. *Nat. Photonics* **2008**, *2*, 351–354.
39. Englund, D.; Fattal, D.; Waks, E.; Solomon, G.; Zhang, B.; Nakaoka, T.; Arakawa, Y.; Yamamoto, Y.; Vuckovic, J. Controlling the Spontaneous Emission Rate of Single Quantum Dots in a Two-Dimensional Photonic Crystal. *Phys. Rev. Lett.* **2005**, *95*, 013904–013908.
40. Yeh, D. M.; Huang, C. F.; Chen, C. Y.; Lu, Y. C.; Yang, C. C. Surface Plasmon Coupling Effect in an InGaN/GaN Single-Quantum-Well Light-Emitting Diode. *Appl. Phys. Lett.* **2007**, *91*, 171103–171106.
41. Yeh, D. M.; Huang, C. F.; Chen, C. Y.; Lu, Y. C.; Yang, C. C. Localized Surface Plasmon-Induced Emission Enhancement of a Green Light-Emitting Diode. *Nanotechnology* **2008**, *19*, 345201–345205.
42. Eichelbaum, M.; Rademann, K. Plasmonic Enhancement or Energy Transfer? On the Luminescence of Gold-, Silver-, and Lanthanide-Doped Silicate Glasses and Its Potential for Light-Emitting Devices. *Adv. Funct. Mater.* **2009**, *19*, 2045–2052.
43. Paz-Soldan, D.; Lee, A.; Thon, S. M.; Adachi, M. M.; Dong, H.; Maraghechi, P.; Yuan, M.; Labelle, A. J.; Hoogland, S.; Liu, K.; *et al.* Jointly Tuned Plasmonic-Excitonic Photovoltaics Using Nanoshells. *Nano Lett.* **2013**, *13*, 1502–1508.
44. Khon, E.; Mereshchenko, A.; Tarnovsky, A.; Acharya, K.; Klinkova, A.; Hewa-Kasakarage, N.; Nemitz, I.; Zamkov, M. Suppression of the Plasmon Resonance in Au/CdS Colloidal Nanocomposites. *Nano Lett.* **2011**, *11*, 1792–1799.
45. Korobchevskaya, K.; George, C.; Manna, L.; Comin, A. Effect of Morphology on Ultrafast Carrier Dynamics in Asymmetric Gold−Iron Oxide Plasmonic Heterodimers. *J. Phys. Chem. C* **2012**, *116*, 26924–26928.
46. Guardia, P.; Korobchevskaya, K.; Casu, A.; Genovese, A.; Manna, L.; Comin, A. Plasmon Dynamics in Colloidal Au_2Cd Alloy−CdSe Core/Shell Nanocrystals. *ACS Nano* **2013**, *7*, 1045–1053.
47. Kobayashi, Y.; Nonoguchi, Y.; Wang, L.; Kawai, T.; Tamai, N. Dual Transient Bleaching of Au/PbS Hybrid Core/Shell Nanoparticles. *J. Phys. Chem. Lett.* **2012**, *3*, 1111–1116.
48. Sagarzazu, G.; Inoue, K.; Saruyama, M.; Sakamoto, M.; Teranishi, T.; Masuoa, S.; Tamai, N. Ultrafast Dynamics and Single Particle Spectroscopy of Au−CdSe Nanorods. *Phys. Chem. Chem. Phys.* **2013**, *15*, 2141–2152.
49. Mongin, D.; Shaviv, E.; Maioli, P.; Crut, A.; Banin, U.; Del Fatti, N.; Valleé, F. Ultrafast Photoinduced Charge Separation in Metal Semiconductor Nanohybrids. *ACS Nano* **2012**, *6*, 7034–7043.
50. Mie, G. Contributions to the Optics of Diffuse Media, Especially Colloid Metal Solutions. *Ann Phys.* **1908**, *25*, 377–445.
51. Klimov, V.; Hunsche, S.; Kurz, H. Biexciton Effects in Femtosecond Nonlinear Transmission of Semiconductor Quantum Dots. *Phys. Rev. B* **1994**, *50*, 8110–8113.
52. Hunsche, S.; Dekorsy, T.; Klimov, V.; Kurz, H. Ultrafast Dynamics of Carrier-Induced Absorption Changes in Highly-Excited CdSe Nanocrystals. *Appl. Phys. B: Lasers Opt.* **1996**, *62*, 3–10.
53. Vill, V.; Peters, G.; Sajus, H. *Compounds with 13 to 100 Carbon Atoms*; Springer-Verlag: Berlin Heidelberg, 1998.
54. Dinger, A.; Petillon, S.; Grün, M.; Hetterich, M.; Klingshirn, C. Conduction Band Offset of the CdS/ZnSe Heterostructure. *Semicond. Sci. Technol.* **1999**, *14*, 595–598.
55. Hewa-Kasakarage, N. N.; El-Khoury, P. Z.; Tarnovsky, A. N.; Kirsanova, M.; Nemitz, I.; Nemchinov, A.; Zamkov, M. Ultrafast Carrier Dynamics in Type II ZnSe/CdS/ZnSe Nanobarbells. *ACS Nano* **2010**, *4*, 1837–1844.
56. Ahmadi, T. S.; Logunov, S. L.; El-Sayed, M. A. Picosecond Dynamics of Colloidal Gold Nanoparticles. *J. Phys. Chem.* **1996**, *100*, 8053–8056.
57. Logunov, S. L.; Ahmadi, T. S.; El-Sayed, M. A.; Khoury, J. T.; Whetten, R. L. Electron Dynamics of Passivated Gold Nanocrystals Probed by Subpicosecond Transient Absorption Spectroscopy. *J. Phys. Chem. B* **1997**, *101*, 3713–3719.
58. Voisin, C.; Del Fatti, N.; Christofilos, D.; Vallée, F. Ultrafast Electron Dynamics and Optical Nonlinearities in Metal Nanoparticles. *J. Phys. Chem. B* **2001**, *105*, 2264–2280.
59. Lo, S. S.; Shi, H. Y.; Huang, L.; Hartland, G. V. Imaging the Extent of Plasmon Excitation in Au Nanowires Using Pump-Probe Microscopy. *Opt. Lett.* **2013**, *38*, 1265–1267.
60. Link, S.; Burda, C.; Mohamed, M. B.; Nikoobakht, B.; El-Sayed, M. A. Femtosecond Transient-Absorption Dynamics of Colloidal Gold Nanorods: Shape Independence of the Electron-Phonon Relaxation Time. *Phys. Rev. B* **2000**, *61*, 6086–6090.
61. Aruda, K. O.; Tagliazucchi, M.; Sweeney, C. M.; Hannah, D. C.; Weiss, E. A. The Role of Interfacial Charge Transfer-Type Interactions in the Decay of Plasmon Excitations in Metal Nanoparticles. *Phys. Chem. Chem. Phys.* **2013**, *15*, 7441–7449.
62. Mokari, T.; Rothenberg, E.; Popov, I.; Costi, R.; Banin, U. Selective Growth of Metal Tips onto Semiconductor Quantum Rods and Tetrapods. *Science* **2004**, *304*, 1787–1790.
63. Shore, M. S.; Wang, J.; Johnston-Peck, A. C.; Oldenburg, A. L.; Tracy, J. B. Synthesis of Au(Core)/Ag(Shell) Nanoparticles and their Conversion to AuAg Alloy Nanoparticles. *Small* **2011**, *7*, 230–234.
64. Hewa-Kasakarage, N. N.; Kirsanova, M.; Nemchinov, A.; Schmall, N.; El-Khoury, P. Z.; Tarnovsky, A. N.; Zamkov, M. Radiative Recombination of Spatially Extended Excitons in (ZnSe/CdS)/CdS Heterostructured Nanorods. *J. Am. Chem. Soc.* **2009**, *131*, 1328–1334.